

JUNG-UK LEE<sup>1</sup>, YOUNG-KYUN KIM<sup>2</sup>, SEONG-MOON SEO<sup>2</sup>, KEE-AHN LEE<sup>1\*</sup>

## HIGH TEMPERATURE OXIDATION PROPERTY OF Ni BASED SUPERALLOY CM247LC PRODUCED VIA SELECTIVE LASER MELTING PROCESS

CM247LC alloy was manufactured by using selective laser melting (SLM) process, one of the laser powder bed fusion (L-PBF) methods. The hot isostatic pressing (HIP) process was additionally conducted on the SLM-built CM247LC to control its microstructures and defects. The high temperature oxidation property was investigated, and it was compared with conventional DS247LC sample (reference) prepared via the directional solidification process. The L-PBF HIP sample showed blocky-type MC carbides generated along the grain boundary with average size of about 200 nm. A semi-spherical primary  $\gamma'$  phase of size 0.4-1.0  $\mu\text{m}$  was also observed inside the grains. Moreover, the DS247LC sample displayed a coarse eutectic  $\gamma'$  phase and many script-type MC carbides. Furthermore, cuboidal-type  $\gamma'$  with an average size of about 0.5  $\mu\text{m}$  was detected. High-temperature oxidation tests were conducted at 1000°C and 1100°C for 24 hours. The results at 1100°C oxidation temperature showed that the measured oxidation weight gains for HIP and DS247LC were 1.96 mg/cm<sup>2</sup> and 2.26 mg/cm<sup>2</sup>, respectively, indicating the superior high-temperature oxidation resistance of the L-PBF HIP sample. Based on the above results, a high-temperature oxidation mechanism of the CM247LC alloys manufactured by the SLM process and the directional solidification process has been proposed.

*Keywords:* Ni-based superalloy; Selective laser melting; Directional solidification; Microstructure; High temperature oxidation property

### 1. Introduction

Ni-based superalloys are used as materials for aircraft parts, such as turbine blades, turbine disks, and vanes because of their excellent mechanical properties in extreme environments, especially at very high temperatures, and corrosion and oxidation resistance [1,2]. When Ni is used as a matrix, CM247LC exhibits excellent physical properties in different applications, such as in solid solution strengthening with added elements, viz. W, Co, and Cr, in precipitation hardening via carbide formation, and in another precipitation hardening to generate  $\gamma'$  phase [Ni<sub>3</sub>Al] using the Al element [3,4]. In particular, it is possible to obtain a  $\gamma'$  phase with 65% volume fraction using heat treatment and high Al content [5]. The  $\gamma'$  phase produced has an L1<sub>2</sub> structure with <2% mismatch with the  $\gamma$  matrix, and when potential passes through the  $\gamma'$  phase, an anti-phase boundary (APB) is formed to reinforce the alloy [6,7]. Ezugwu et al. [8] reported that such Ni-based superalloys have low machinability due to high concentration of the refractory element and complex precipitation strengthening, resulting in limitations in controlling complex

shapes. As developments in the aerospace field require more parts with complex shapes and optimized high-temperature, extensive research to produce Ni-based superalloys using additive manufacturing (AM) is going on for the past 10 years [9,10].

AM is a process that can control the formation of complex three-dimensional shapes, as desired by consumers, by contiguously stacking powders [11,12]. The powder bed fusion-based selective laser melting (SLM) process features high cooling rate and excellent shape design freedom compared to other AM processes [13]. However, most studies on AM technology related to Ni-based superalloys have focused on manufacturing, microstructure, mechanical properties, and deformation mechanism of IN625 and IN718 Ni-based superalloys. Therefore, there is a need for research that can be applied to aviation parts (turbine blade, turbine disk, vane) by highlighting the advantages of the SLM process to CM247LC, which can show excellent physical and chemical properties at higher temperatures.

In the present study, the SLM process has been employed to manufacture Ni-based superalloy CM247LC. The possibility as an alternative process was confirmed by controlling defects and

<sup>1</sup> INHA UNIVERSITY, DEPARTMENT OF MATERIALS SCIENCE AND ENGINEERING, INCHEON 22212, REPUBLIC OF KOREA

<sup>2</sup> KOREA INSTITUTE OF MATERIALS SCIENCE, CHANGWON 51508, REPUBLIC OF KOREA

\* Corresponding author: keeahn@inha.ac.kr



microstructure through hot isostatic pressing, which is a post-treatment process. Furthermore, high-temperature oxidation characteristics were investigated using CM247LC alloy manufactured by the conventional directional-solidification process, as a comparative material. Based on the experimental results, a high-temperature oxidation mechanism of SLM CM247LC was also suggested.

## 2. Experimental

Table 1 shows the chemical composition of the powders used in this study, as obtained using an inductively coupled plasma (ICP) spectrometer.

TABLE 1

Chemical composition of CM247LC powders used in this study

Element	Ni	W	Co	Cr	Al	Ta	Hf	Ti	Mo	C
wt.%	Bal.	9.4	9.2	8.3	5.5	3.2	1.5	0.8	0.58	0.08

The specimen CM247LC was formed via SLM process under optimal process conditions, obtained from the pre-tests. The process conditions included the islands chessboard scanning pattern (i.e., raster at 90° angle rotation for each layer), laser power ( $P$ ) of 90 W, laser scanning speed ( $v$ ) of 600 mm/s, hatch spacing ( $h$ ) of 100  $\mu\text{m}$ , layer thickness ( $t$ ) of 25  $\mu\text{m}$  to fabricate a bar-type specimen sized 10 mm  $\times$  10 mm  $\times$  75 mm. To express direction, we used building direction (BD) and transverse direction (TD), separately. For defect and microstructure control of the SLM-built CM247LC, hot isostatic press (HIP) process was performed under the following conditions: the pressure was 150 MPa, temperature 1200°C (heating rate of 13°C/min), duration was 4 hours, and a sample cooling rate was 10°C/min (to be named SLM-HIP sample). Another CM247LC (to be named DS247LC sample) was manufactured via the conventional directional-solidification route and used to compare with the SLM CM247LC. Standard heat treatment (1232°C/2h + 1079°C/4h + 871°C/20h) was performed on both the materials. XRD (Ultima IV, scan step size; 0.01 deg., scan rate; 1 deg./min, 2 $\theta$ ; 30-100 deg.) was used for phase analysis of the CM247LC alloys. An optical microscope (OM, Olympus BX53M) was used to measure the porosity, cracks, and macro image analysis. Subsequent element distribution and crystal orientation analysis was performed using electron backscatter diffraction (EBSD, Nordlys nano detector). Meanwhile, microstructures were observed using field-emission scanning electron microscopy (FE-SEM, TESCAN MIRA 3). Oxidation tests were conducted at 1000°C and 1100°C for 24 hours to examine the high-temperature oxidation properties. For this, a thermal gravimetry analysis system (TGA, Rigaku TG-DTA 8122) was used in which 79% N<sub>2</sub> + 21% O<sub>2</sub> gas, similar to atmospheric environment, at 100 mL/min. flow rate was employed, The oxidation specimens used in this study were of size 4 mm  $\times$  4 mm  $\times$  4 mm and polished with silicon carbide papers and diamond suspension. The heating rate to the

specified temperature was set at 10°C/min. After oxidation tests, the cross-sections of oxidized samples were analyzed using an electron probe X-ray microanalyzer (EPMA, Jeol, JXA-8500F).

## 3. Results and discussion

### 3.1. Material preparation

Fig. 1 shows the shape of the CM247LC alloy manufactured by SLM process (a), XRD analysis results of initial powders and as-built alloy (b), and OM observation images of both alloys (c and d). The powder particles were spherical in shape with an average measured size of 34.5  $\mu\text{m}$  (D10 = 22.7  $\mu\text{m}$ , D50 = 34.0  $\mu\text{m}$ , D90 = 50.8  $\mu\text{m}$ ) (Fig. 1a). XRD analysis results showed the peaks of  $\gamma$  and  $\gamma'$  phases only, and unlike the powder and SLM-HIP sample, the DS247LC sample showed a high peak intensity (200) due to one-way coagulation (Fig. 1b). The microstructures of the TD plane were checked to analyze the defect density of both alloys. In the SLM-HIP sample, only fine closed pores were observed, and image-based analysis confirmed the defect density to be 0.28% (Fig. 1c). The DS247LC sample showed similar levels of defect density, size, and distribution as the SLM-HIP sample (Fig. 1d).

### 3.2. Microstructure of the CM247LC alloys

SEM images of the TD plane (Fig. 2) were taken to closely analyze the microstructure at the intra-grain scale for the two alloys. Examining the SLM-HIP sample at low magnification confirmed the blocky-type MC carbides with an average size of about 200 nm along the grain boundary (Fig. 2a). In general, the MC carbide produced during CM247LC alloying is known as precipitate containing Hf and Ta elements [14]. On the other hand, the DS247LC sample showed a coarse eutectic  $\gamma'$  phase, and many script-type MC carbides (Fig. 2b). At high magnification, the SLM-HIP sample showed MC carbide, with average size 0.3  $\mu\text{m}$ , present along the grain boundaries and presence of a semi-spherical primary  $\gamma'$  phase of size 0.4 to 1.0  $\mu\text{m}$  (Fig. 2c). The  $\gamma'$  volume fraction was measured to be 60.4%. In the DS247LC sample, cuboidal-type  $\gamma'$ , with average size of about 0.5  $\mu\text{m}$  and volume fraction of 62.2%, was found. Yang et al. [15] reported the shape of  $\gamma'$  varied with the difference of cooling rate in a Ni-based superalloy. Therefore, it can be also explained that the difference in the shape of  $\gamma'$  between the SLM-HIP sample and DS247LC sample is mainly due to the difference of cooling rate.

### 3.3. High-temperature oxidation properties of CM247LC alloys

Fig. 3 shows the weight gains of high-temperature oxidation curves at 1000°C and 1100°C. The oxidation weights of

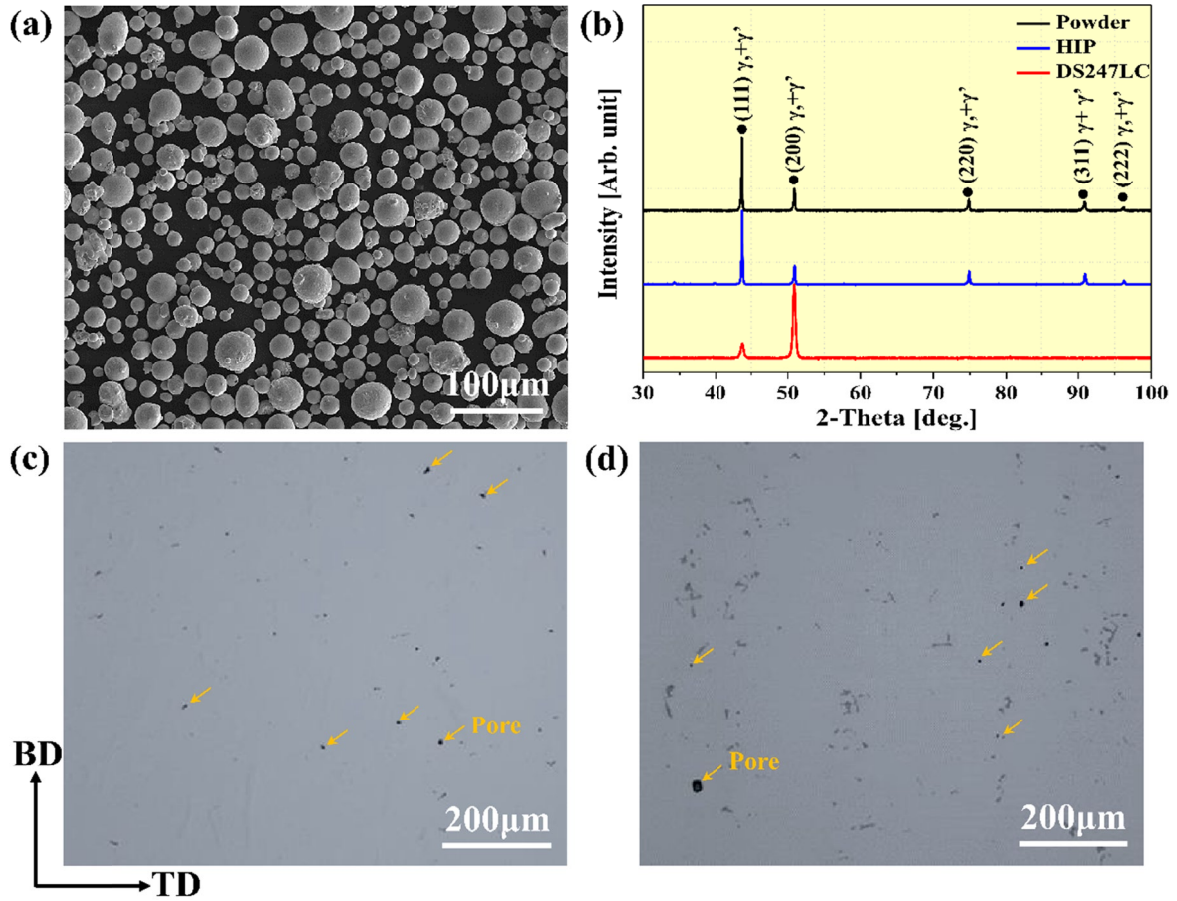


Fig. 1. (a) SEM micrographs of the morphology of the initial CM247LC powders, (b) XRD analysis results and optical micrographs of (c) SLM-HIP sample and (d) DS247LC sample

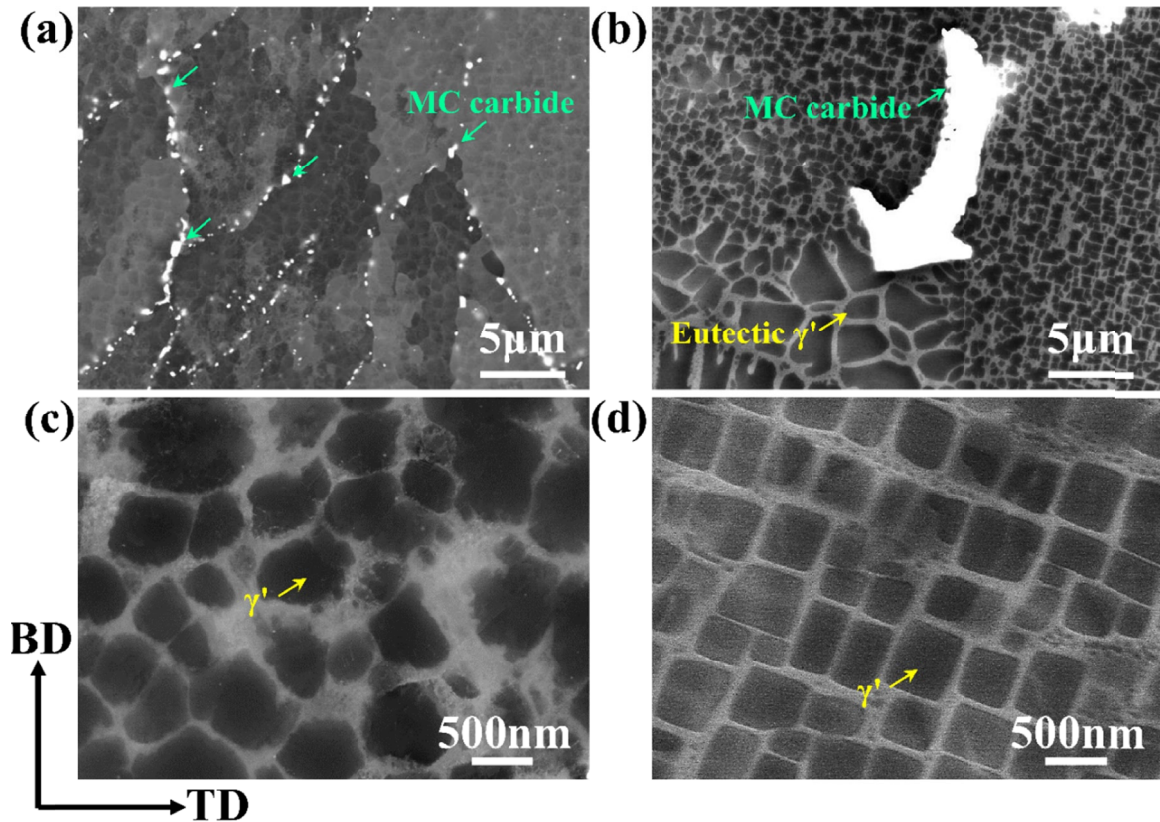


Fig. 2. SEM observation results showing the precipitates in CM247LC: (a,c) SLM-HIP sample, (b,d) DS247LC sample

both the materials displayed a parabolic shape curve with time. Moreover, the weight gain showed a general tendency of increasing with increase in the oxidation temperature. In general, when a thermodynamically stable and dense oxide layer ( $\text{Al}_2\text{O}_3$ ,  $\text{Cr}_2\text{O}_3$ ) is formed in a Ni-based superalloy, the weight gain curve over time is typically parabolic in shape [16,17]. The oxidation weight gains of the SLM-HIP and DS247LC samples at  $1000^\circ\text{C}$  after 24 hours were  $0.88 \text{ mg/cm}^2$  and  $1.21 \text{ mg/cm}^2$ , respectively. At  $1100^\circ\text{C}$ , they were  $1.96 \text{ mg/cm}^2$  and  $2.26 \text{ mg/cm}^2$ , indicating that the difference in oxidation weight gains of the two alloys was larger at  $1100^\circ\text{C}$ . It can be also noted that the SLM-HIP sample showed relatively better oxidation resistance at both the temperatures.

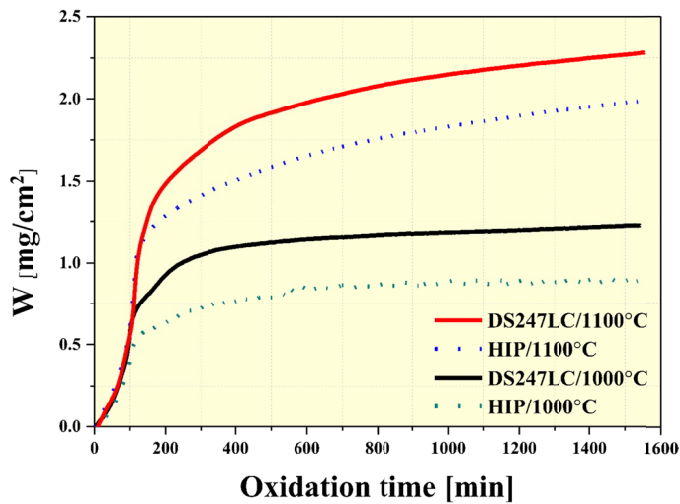


Fig. 3. High temperature oxidation curves of SLM-HIP sample and DS247LC sample at  $1000^\circ\text{C}$  and  $1100^\circ\text{C}$  for 24 hours

For materials that follow the parabolic law in the oxidation curve, the relationship between the weight gain and oxidation time can be expressed by the following equation [18].

$$W = (Kp \times t)^{\frac{1}{2}} \quad (1)$$

where,  $W$  refers to the mass gain,  $Kp$  refers to the parabolic rate (oxidation rate), and  $t$  refers to the oxidation time. As a result of calculating the parabolic rate, the  $Kp$  [ $\text{mg}^2/\text{cm}^4 \times \text{s}^{-1}$ ] values of SLM-HIP sample and DS247LC sample were obtained as  $8.96 \times 10^{-6}$  and  $16.9 \times 10^{-6}$  at  $1000^\circ\text{C}$ , and  $4.44 \times 10^{-5}$  and  $5.91 \times 10^{-5}$  at  $1100^\circ\text{C}$ , respectively. At  $1100^\circ\text{C}$ , the measured parabolic rate of the DS247LC sample was found to be about 1.3 times higher (lower oxidation resistance) than that of the SLM-HIP sample.

### 3.4. High-temperature oxidation mechanism of SLM-HIP CM247LC alloy

To understand the mechanism of oxide formation behavior, cross-sectional EPMA study was done (Fig. 4). Vertical cross-sections of the two materials after oxidation at  $1100^\circ\text{C}$  showed

that oxide formed densely in the metal surface. The SLM-HIP and DS247LC samples had average oxidation layer thickness values of  $4.9 \mu\text{m}$  and  $5.3 \mu\text{m}$ , respectively, indicating that the DS247LC sample possessed a thicker oxide layer. The oxide was formed at the metal interface in the order  $\text{Al}_2\text{O}_3$ ,  $\text{Cr}_2\text{O}_3$ , and NiO. Moreover, both the samples generated many inner oxides of HfO inside the metal region.  $\text{Al}_2\text{O}_3$  is known as the oxide that affects the most for the high-temperature oxidation properties of CM247LC alloy [19,20]. Al in elemental state diffuses into the  $\gamma'$  having the  $\text{Ni}_3\text{Al}$  structure at the beginning of high-temperature oxidation. It then binds with the external O element to form a stable  $\text{Al}_2\text{O}_3$  passivation film and exhibits excellent high-temperature oxidation resistance. An Al depletion zone is created at this time. The Al depletion zones are the two oxidized SLM-HIP and DS247LC samples were measured as  $8.6 \mu\text{m}$  and  $11.7 \mu\text{m}$ , respectively, indicating that the DS247LC sample had broader depletion zones. The oxidized DS247LC sample had a wider Al depletion zone, and it also had a thick oxide layer, indicating that relatively non-uniform  $\text{Al}_2\text{O}_3$  layers were formed to trigger additional oxidation during high-temperature oxidation. The oxidation process was mainly influenced by the internal penetration of oxygen atoms, and the diffusion of solute elements [21]. Therefore, when the same amount of oxygen is supplied, the weight gain rate was significantly affected by the transportation rate of the solute elements, and grain boundaries (GBs) or sub-structures acted as diffusion paths [22,23]. Mallikarjuna et al. [24] reported that the  $\gamma$  channel acted as an Al diffusion path. In other words, many GBs and a higher fraction of the  $\gamma$  channel of the SLM-HIP sample observed in the initial microstructure acted as the diffusion path for the Al and O elements to form stable  $\text{Al}_2\text{O}_3$  rapidly at the initial stage of the high-temperature oxidation, exhibiting better high-temperature oxidation resistance than the DS247LC sample.

## 4. Conclusions

In the present study, CM247LC was manufactured via the SLM process and HIP post-treatment process was performed. The SLM-HIP CM247LC was then compared with the DS247LC sample produced by the conventional directional-solidification process. The microstructure and high-temperature oxidation properties of the CM247LC were examined and the following conclusions can be drawn.

1. The oxidation weight gains of the SLM-HIP and DS247LC samples at  $1000^\circ\text{C}$  after 24 hours were  $0.88 \text{ mg/cm}^2$  and  $1.21 \text{ mg/cm}^2$ , respectively. They were  $1.96 \text{ mg/cm}^2$  and  $2.26 \text{ mg/cm}^2$  at  $1100^\circ\text{C}$ , indicating that the high temperature oxidation resistance of the SLM-HIP sample was relatively better at both the oxidation temperatures.
2. It was suggested that the superior high-temperature oxidation resistance of the SLM-HIP sample was due to many GBs and a large fraction of the  $\gamma$  channels acted as the diffusion paths for the Al and O elements for the dense formation of  $\text{Al}_2\text{O}_3$  at the initial stage of oxidation.

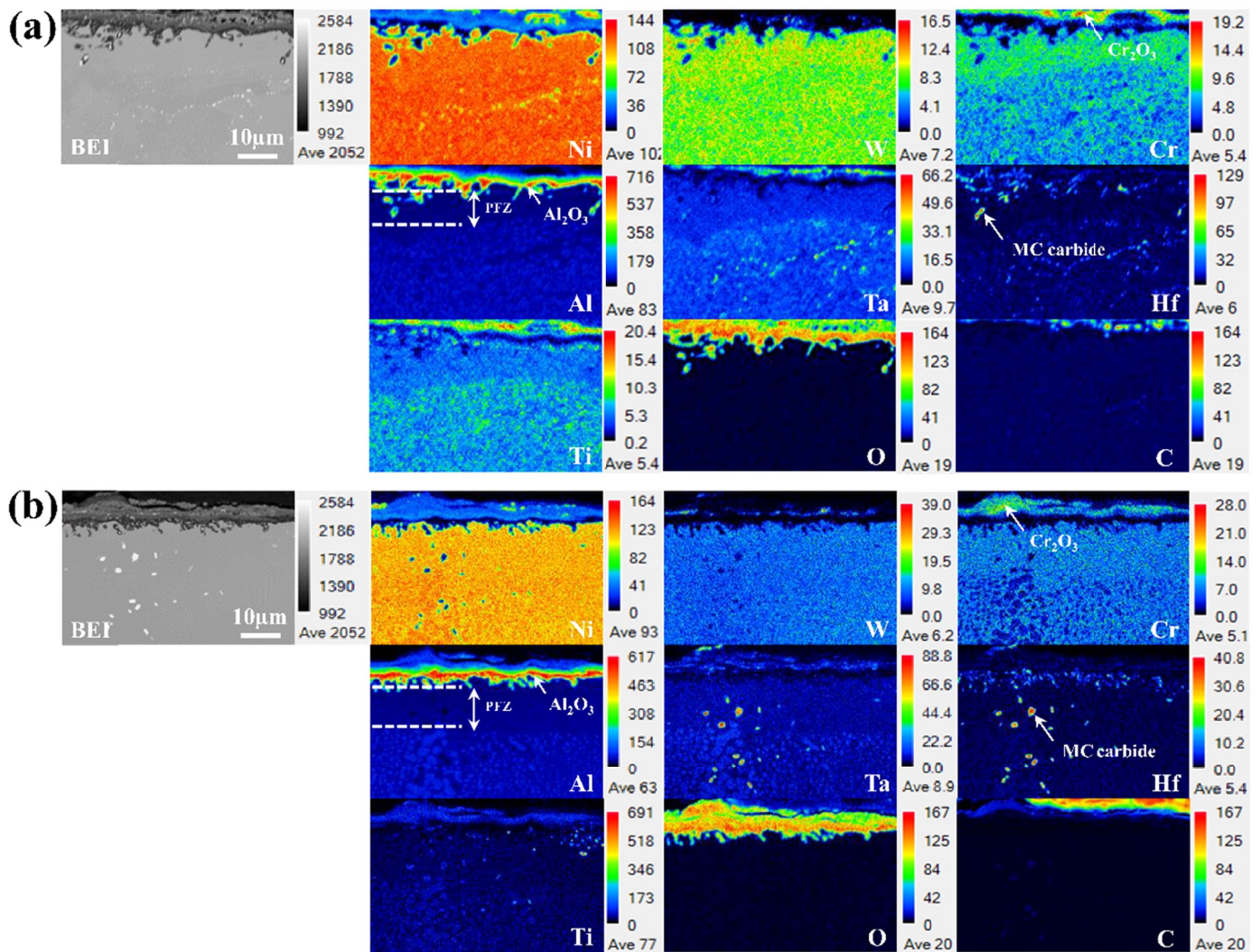


Fig. 4. EPMA analysis of results the cross-sections after oxidation at 1100°C: (a) SLM-HIP sample, (b) DS247LC sample

#### Acknowledgments

This work was supported by the Korea Evaluation Institute of Industrial Technology (KEIT) and the Ministry of Trade, Industry & Energy (MOTIE) of the Republic of Korea (No. 20011103).

#### REFERENCES

- [1] P. Liu, R. Zhang, Y. Yuan, C. Cui, Y. Zhou, X. Sun, *J. Alloys Compd.* **831**, 154618 (2020).
- [2] C.L. Yang, Z.J. Zhang, P. Zhang, C.Y. Cuic, Z.F. Zhang, *Mater. Sci. Eng. A* **736**, 100-104 (2018).
- [3] L.N. Carter, C. Martin, P. J. Withers, M. M. Attallah, *J. Alloys Compd.* **615**, 338-347 (2014).
- [4] M. Chiou, S. Jian, A. Yeh, C. Kuo, J. Juang, *Mater. Sci. Eng. A* **655**, 237-243 (2016).
- [5] I.S. Kim, B.G. Choi, J.E. Jung, J.H. Do, W.Y. Seok, Y.H. Lee, I.Y. Jeong, *Mater. Character.* **165**, 110378 (2020).
- [6] J. Tiley, G.B. Viswanathan, J.Y. Hwang, A. Shiveley, R. Banerjee, *Mater. Sci. Eng. A* **528**, 32-36 (2010).
- [7] L. Heep, C. Schwalbe, C. Heinze, A. Dlouhy, C.M.F. Rae, G. Egeler, *Scripta.* **190**, 121-125 (2021).
- [8] E.O. Ezugwu, E.M. Wang, A.R. Machado, *J. Mater. Process. Technol.* **86**, 1-16 (1999).
- [9] S. Griffiths, H. Ghasemi Tabasi, T. Ivas, X. Maeder, A. De Luca, K. Zwiackner, R. Wróbel, J. Jhabvala, R.E. Logé, C. Leinenbach, *Addit. Manuf.* **36**, 101443 (2020).
- [10] S. Catchpole-Smith, N. Aboulkhair, L. Parry, C. Tuck, I.A. Ashcroft, A. Clare, *Addit. Manuf.* **15**, 113-122 (2017).
- [11] R.M. Moreno, V.D. Divya, S.L. Driver, O.M.D.M. Messé, T. Ilston, S. Baker, M.A. Carpenter, H.J. Stone, *Mater. Sci. Eng. A* **674**, 529-539 (2016).
- [12] N.J. Harrison, I. Todd, K. Mumtaz, *Acta.* **94**, 59-68 (2015).
- [13] W.M. Tucho, V.H. Lysne, H. Austbø, A. S. Kverneland, V. Hansen, *J. Alloys Compd.* **740**, 910-925 (2018).
- [14] X. Wang, L. N. Carter, B. Pang, M. M. Attallah, M. H. Loretto, *Acta Mater.* **128**, 87-95 (2017).
- [15] A. Yang, Y. Xiong, L. Liu, *Sci. Technol. Adv. Mater.* **2**, 105-107 (2001).
- [16] Y.J. Kang, S.S. Yang, Y.K. Kim, B. AlMangour, K.A. Lee, *Corr. Sci.* **158**, 108082 (2019).

- [17] F.H. Latief, K. Kakehi, X. Fu, *Int. J. Electrochem. Sci.* **7**, 7608-7618 (2012).
- [18] Y.K. Kim, J.H. Kim, Y.J. Kim, D.N. Seidman, K.A. Lee, *Corr. Sci.* **174**, 108833 (2020).
- [19] M.S. Chiou, A.C. Yeh, S.R. Jian, C.M. Kuo, *Adv. Mat. Res.* **922**, 61-66 (2014).
- [20] M.S. Chiou, S.R. Jian, A.C. Yeh, C.M. Kuo, *Int. J. Electrochem. Sci.* **10**, 5981-5993 (2015).
- [21] M. Dressler, M. Nofz, I. Dörfel, R. Saliwan-Neumann, *Thin Solid Films* **520**, 4344-4349 (2012).
- [22] Y. Luo, B. Zhang, Z. Song, C. Li, G. Chen, G. Zhang, *J. Mater. Res.* **35**, 2036-2045 (2020).
- [23] J. Ma, W. Jiang, J. Wang, Y. Zhang, Z. Zhang, *Sci. Rep.* **10**, 1-9 (2020).
- [24] H.T. Mallikarjuna, W.F. Caley, N.L. Richards, *Corr. Sci.* **147**, 394-405 (2019).